Supplementary Information (SI) for Journal of Materials Chemistry A.

Supplementary information

Highly stable PdO nanostructures self-supported on conductive polyaniline nanotubes enable extensive electrochemical hydrogen evolution

Praduman Kumar Gupta,[a] Rajkumar Jana,[b] Puspendu Das,[a] Ayan Datta[b] and Sudip Malik*[a]

[a] School of Applied and Interdisciplinary Science, Indian Association for the Cultivation of Science, Kolkata 700032, India.

[b] School of Chemical Science, Indian Association for the Cultivation of Science, Kolkata 700032, India.

E-mail: psusm2@iacs.res.in

Table of Content:

1. Preparation of samples

Table-S1 Preparation of samples with various concentration of Pd $(NO_3)_2$ with fixed amount of PANI_NT (100mg), with ICP-OES.

Samples	*Conc. Pd $(NO_3)_2$ (mM)*	*Pd loading % (ICP-OES)*	*Particle size distribution*	*I_Q/I_B*	*I_{NH}*
PANI_NT	0	0	-	0.76	10
PdO/PANI_NT-03	3	1.71	2.56 ± 0.1	0.85	5.67
PdO/ PANI_NT -05	5	2.68	2.42±0.1	0.89	6.87
PdO/ PANI_NT -10	10	4.15	2.65±0.1	0.96	2.72
PdO/ PANI_NT -15	15	4.35	2.69±0.1	0.91	3.78
PdO/ PANI_NT -20	20	4.57	2.72±0.1	0.97	3.79
Pd/C 10% wt.	-	10.00 (commercial)		-	

FTIR intensities [$I_{Q\ (1570\ cm^{-1})}$ = Quinoid ring intensity, $I_{B\ (1475\ cm^{-1})}$ = Benzenoid intensity, $I_{NH\ (3430\ cm^{-1})}$ = Intensity of NH (intensity of PANI_NT taken as I_{NH} =10)]

2. UV-vis and FT-IR studies]

Aqueous dispersion of PANI_NTs and PdO/PANI_NT show three absorption peaks at 350, 435, and 850 nm (**Fig. S1a**). Benzenoid rings undergo two transitions centered around 350 and 435 nm, for $\pi - \pi^*$, and polaron-π^* transition respectively. A strong peak at 850nm with an extrapolation toward the near IR region is ascribed to π-polaron transition and it is indicating the presence of emeraldine salt form of PANI chains into PdO/PANI_NT. By increasing the concentration of metal nanoparticles on PANI_NTs, this 900nm broad peak is shifted to a lower wavelength and it might be possible due to the formation of PdO NPs onto PANI which enhances the bandgap of π-polaron state of PANI. The characteristic stretching bands in FT-IR spectrum (**Fig. S1b**) at 3430 cm^{-1} for γN-H, 1570 cm^{-1} for γC=C of quinoid rings, 1475 cm^{-1} for γC=C of benzenoid rings, the two repeating units in PANI chains. 1275 cm^{-1} for γC-N of secondary aromatic amine, 1080 cm^{-1} for γC-H aromatic in plane and 798 cm^{-1}, γC-H aromatic out of plane deformation for 1,4 disubstituted benzene are proved the emeraldine salt of PANI formation.

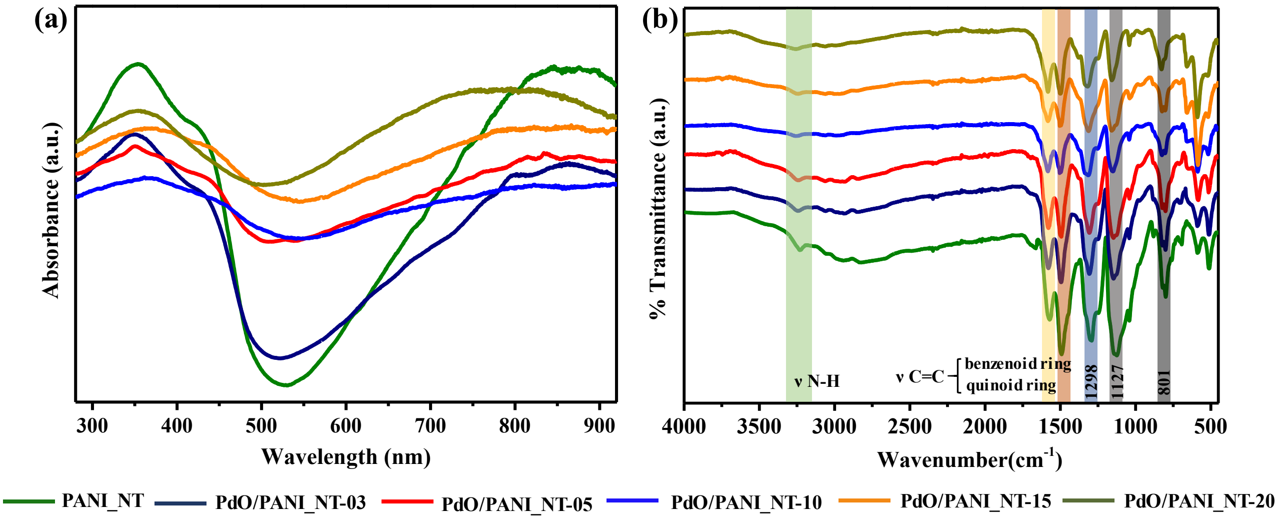

Fig. S1 (a) UV-vis spectra and (b) stretching bands of functional group in FT-IR spectra of PANI_NT and its PdO composites.

3. Structural, Morphological and Compositional studies

The polymerization of aniline with BTCA and APS as dopant acid and oxidant respectively, for the synthesis of PANI_NT, having the diameter ~ 200 nm as remarked in FEG-TEM and FESEM (**Fig.S3**) analysis. Followed by the synthesis of PdO/PANI_NT composites by simply stirring of aqueous nitrate salt of Pd into PANI in room temperature. Pd $(NO_3)_2$ itself has reduced to monodispersed PdO nanoparticles on the surface of nanotubes having average diameter of 2.69 ± 0.1 which is further supported by TEM observations.

Inductively coupled plasma optical-emission spectroscopy (ICP-OES) analysis summarized in Table S1 indicates the percentage of Pd present in the catalysts. An increase in the concentration of Pd salt from 3 to 20 mM leads to increase the loading density of PdO nanoparticles on PANI_NT with having intact morphology, indicting compactness of PdO NPs to PANI chains. For ICP-OES a certain amount of sample was dissolved in aqua regia (3:1 V/V HCl/HNO_3) in a volumetric flask before experiment.

XPS measurement have been conducted in the region of binding energy (E_b) = 50-1200 eV. Survey scan spectra (**Fig. S2a**) have revealed the presence of C, O, N, and Pd. High resolution XPS core-level spectra of C1s and N1s signals at 284.3 and 399.3 eV

Table S2: Structural parameters correlated with simulated database of the PXRD.

	a (Å)	***b (Å)***	***c (Å)***
Simulated PdO PDF No. 01-085-0713	3.030	3.030	5.330
PdO/PANI_NT-15 Experimental data	3.031	3.031	5.335

XPS analysis

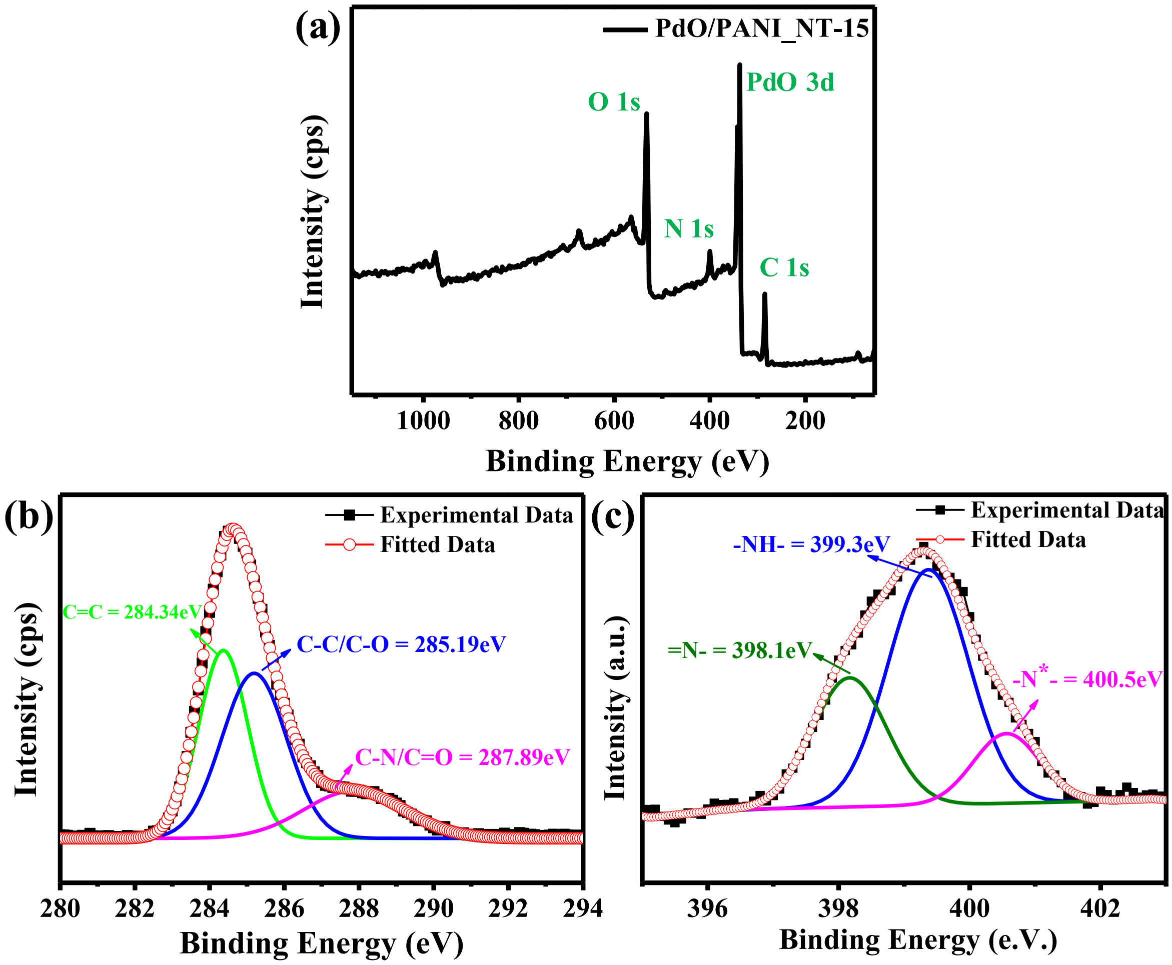

Fig. S2 (a) XPS Survey spectra of PdO/PANI_NT-15, further deconvoluted for (b) C1s and (c) N1s respectively

Morphological studies

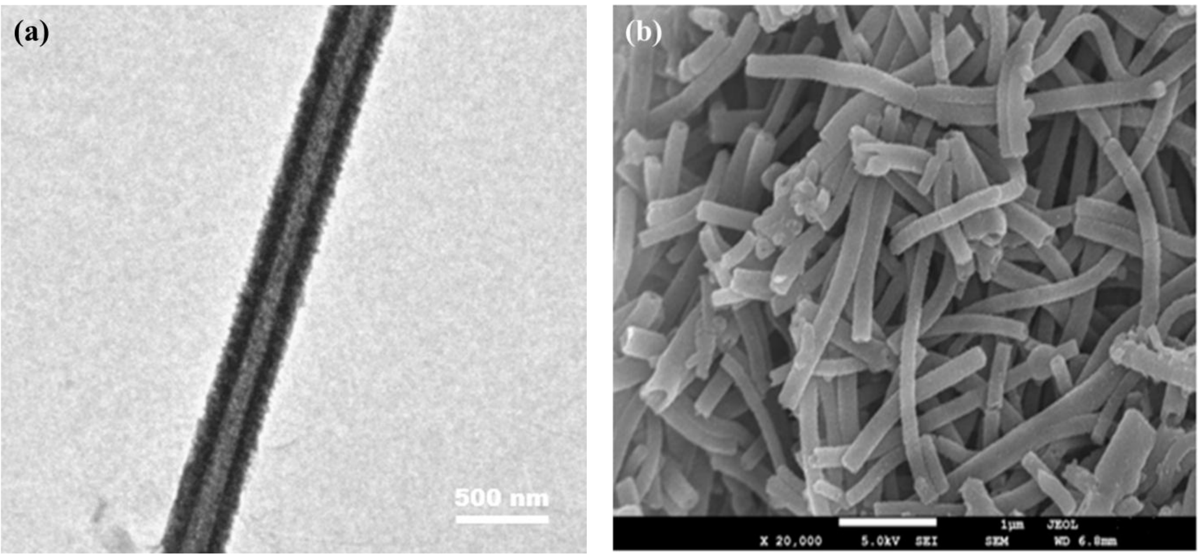

Fig. S3 FEG-TEM and FE-SEM image of synthesized benzene tetracarboxylic acid doped polyaniline (PANI_NT).

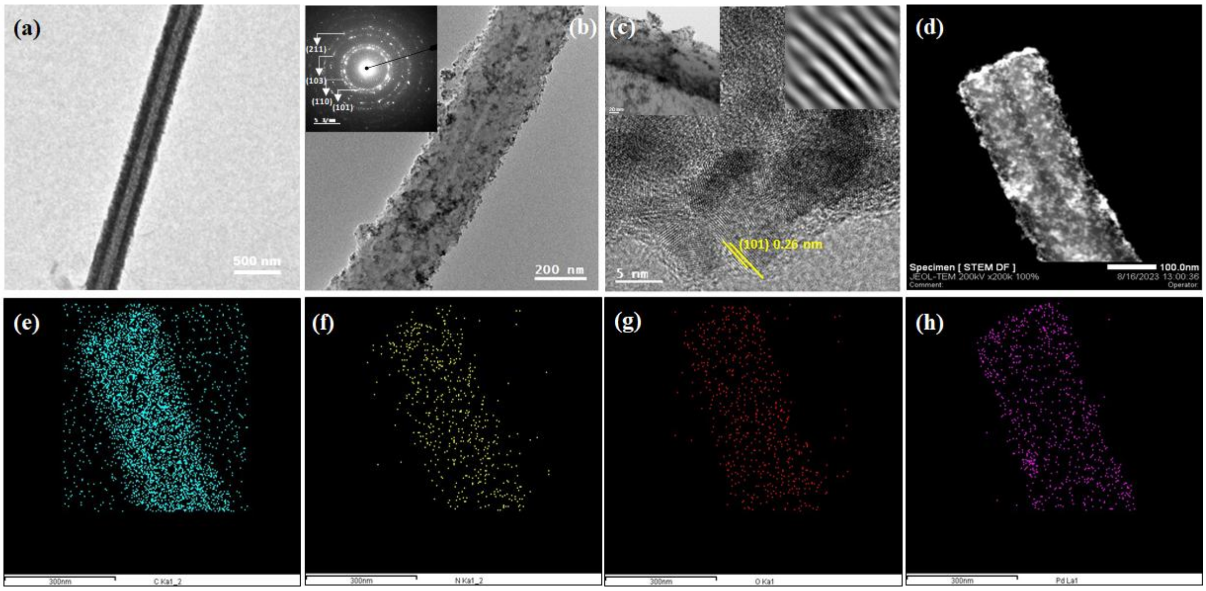

Fig. S4 (a) TEM image of PANI_NT, (b) TEM image (inset: SAED Pattern) of PdO/PANI_NT-15, (c) HRTEM image (inset: close view of nanotube having PdO NPs, magnified lattice fringes) of PdO/PANI_NT-15, (d) HAADF-STEM image, (e) STEM-EDAX elements elemental maps for C, N, O, and Pd of PdO/PANI_NT-15 composite.

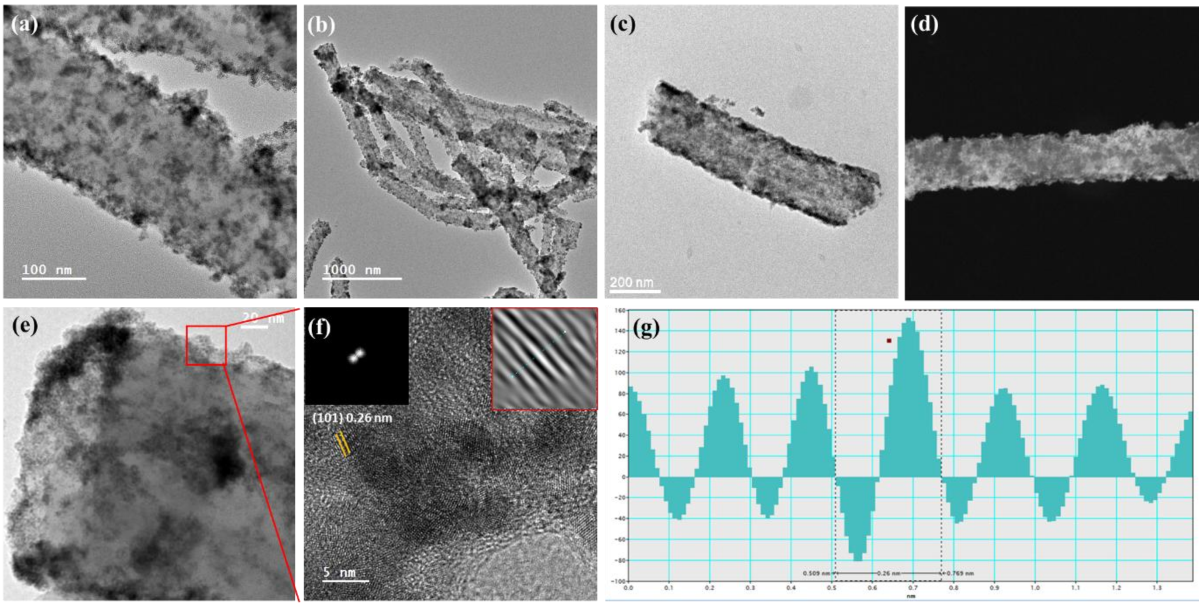

Fig. S5 TEM and HR-TEM images of PdO/PANI_NT-15. (d) HAADF-STEM image. (f), (g) d-spacing corresponds the exposed (101) facet of PdO.

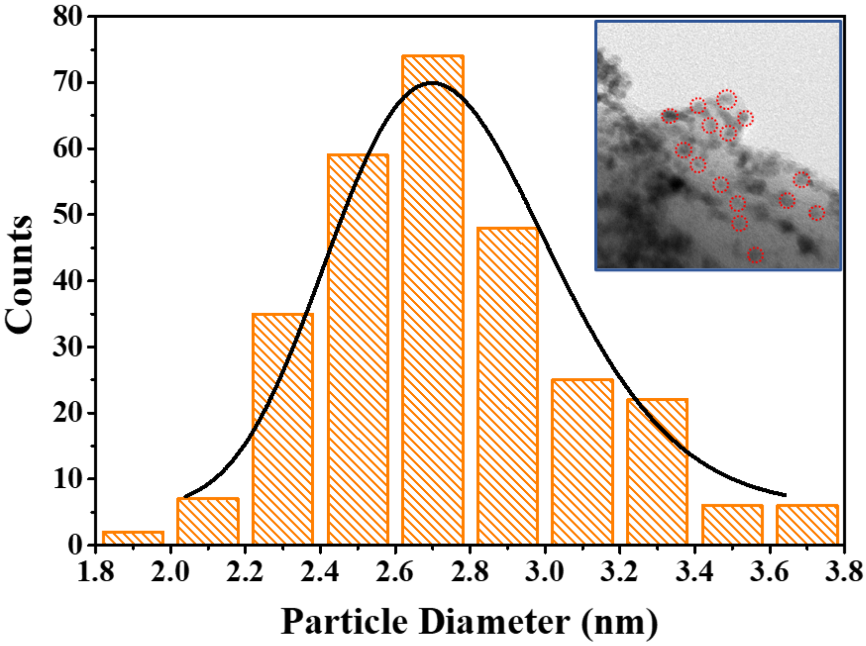

Fig. S6 Particle size distribution of PdO nanoparticles in PdO/PANI_NT-15 composite

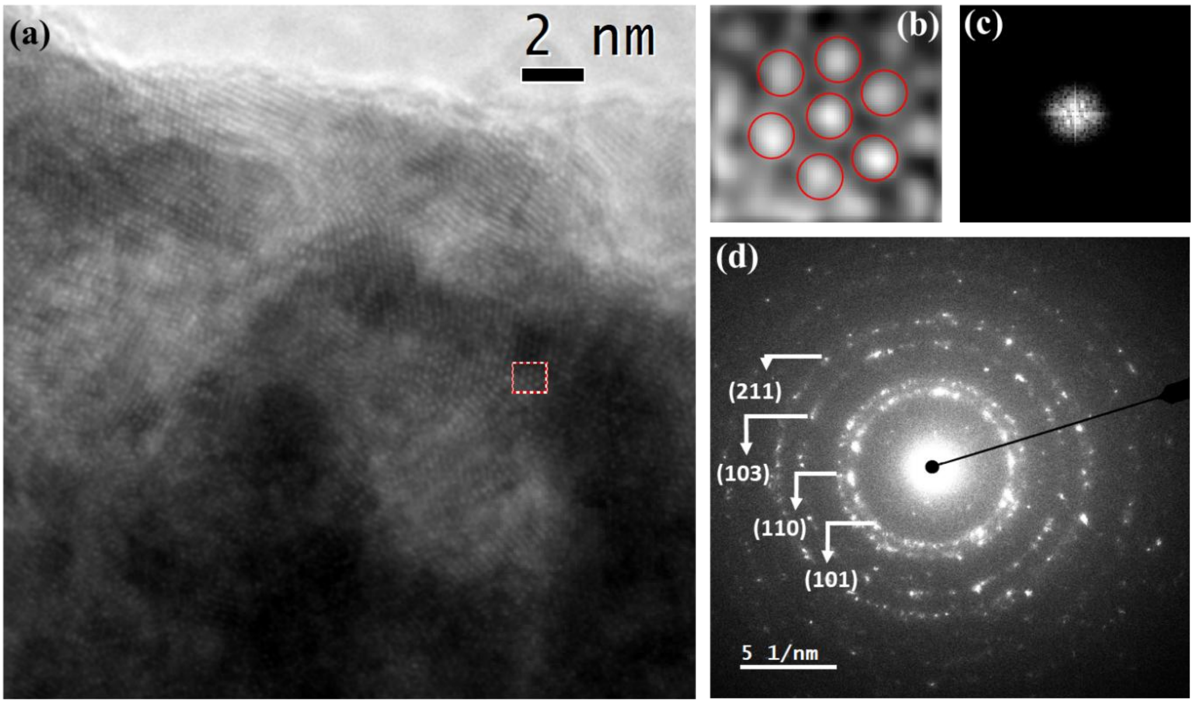

Fig. S7 HR-TEM image of PdO/PANI_NT. (b), (c) lattice structure and (d) SAED pattern of PdO.

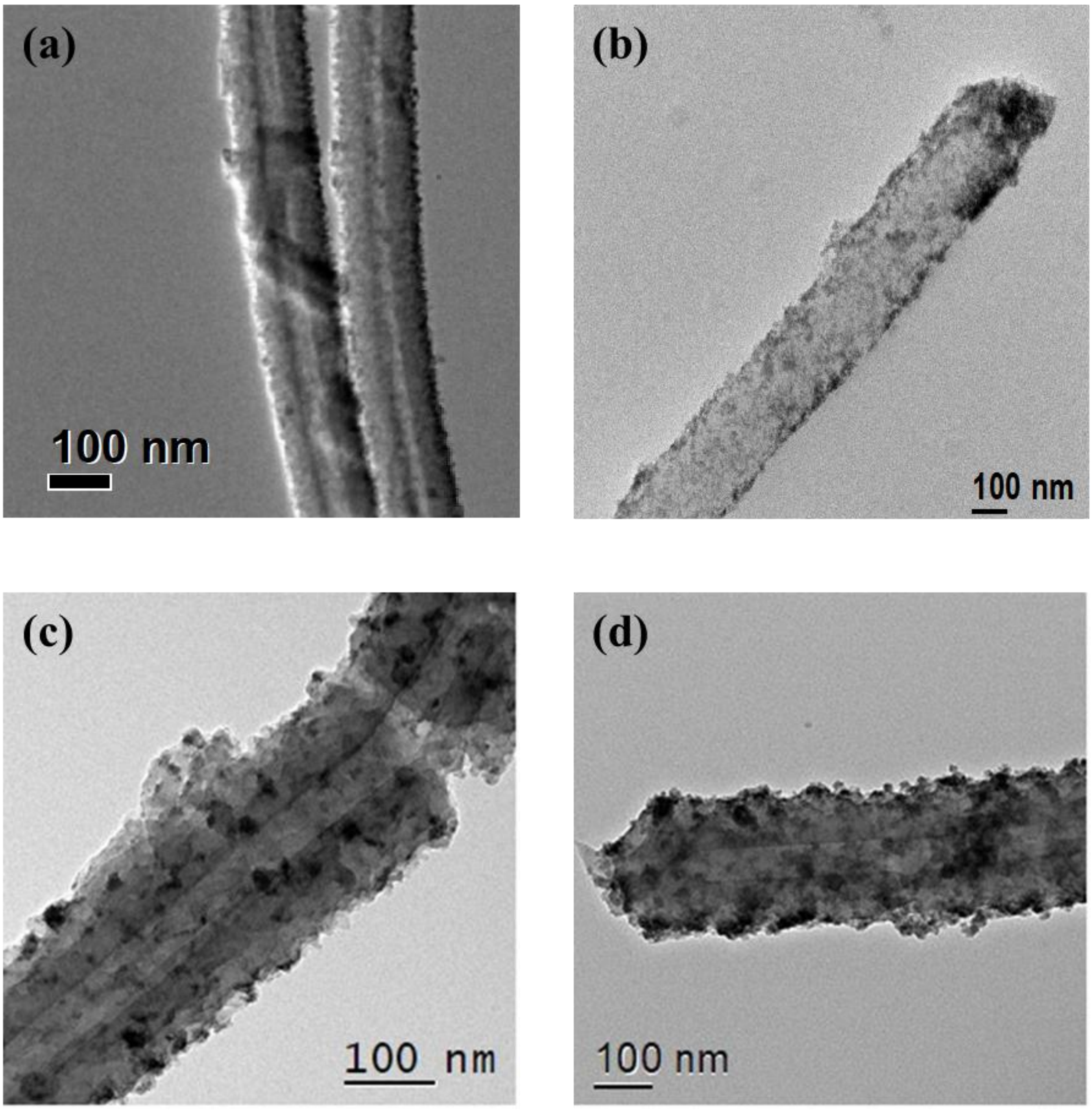

Fig. S8 FEG-TEM images of PdO/PANI_NT-03, PdO/PANI_NT-05, PdO/PANI_NT-10, PdO/PANI_NT-20.

4. Electrochemical Hydrogen Evolution Reaction (HER)

Electrochemical HER performance of all the PdO/PANI_NT catalysts were evaluated in acidic medium in 0.5 M H_2SO_4. The polarization studies of series of sample have been performed with the assistance of linear sweep voltammetry (LSV) techniques with a scan rate of 1 mV s^1 at room temperature. To explore the mechanism of HER, Tafel slope have been ploted against overpotential (η) vs log(J). Based on the classic theory of hydrogen evolution in acidic media, it can be concluded that a Tafel slope of 40 mV indicates that less than 10% of adsorbable hydrogen is covered by the surface, and hydrogen is produced by a Volmer reaction (equation (1)) followed by a rate-determining desorption reaction (equation (2)).

Volmer reaction (adsorption step)

$$H_3O^+ + e^- + \text{cat} \rightleftharpoons \text{cat–}H_{ads}^* + H_2O \qquad \text{(S1)}$$

Heyrovsky reaction (desorption step)

$$H^+ + e^- + \text{cat–}H_{ads}^* \rightleftharpoons H_2 + \text{cat} \qquad \text{(S2)}$$

Tafel reaction (combination step)

$$\text{cat-}H_{ads}^* + \text{cat–}H_{ads}^* \rightleftharpoons H_2 + \text{cat} \qquad \text{(S3)}$$

Reference electrode calibration:

Each potential was calibrated against RHE using aqueous Ag/AgCl as the reference electrode. A Pt wire was used as the working electrode and the counter electrode in 0.5M H_2SO_4 solution saturated with pure hydrogen. At a scan rate of 1 mVs^1, the potential was scanned from -0.1V to -0.4V vs. Ag/AgCl, and **Fig. S9** showed the corresponding cyclic voltammogram. It was determined that the thermodynamic potential for hydrogen electrode reactions was the average of the two potentials at which the current crossed zero. The RHE potential was calculated as

$$E_{(RHE)} = E_{(Ag/AgCl)} + (E^\circ_{(Ag/AgCl)} + 0.0591\times pH) \qquad \text{(S4)}$$

$$E_{(RHE)} = E_{(Ag/AgCl)} + (0.247 + 0.0591\times pH) \qquad (pH=0 \text{ at } 0.5M\ H_2SO_4) \qquad \text{(S5)}$$

$$E(_{RHE}) = E\ (_{Ag/AgCl}) + 0.247\ V \qquad \text{(S6)}$$

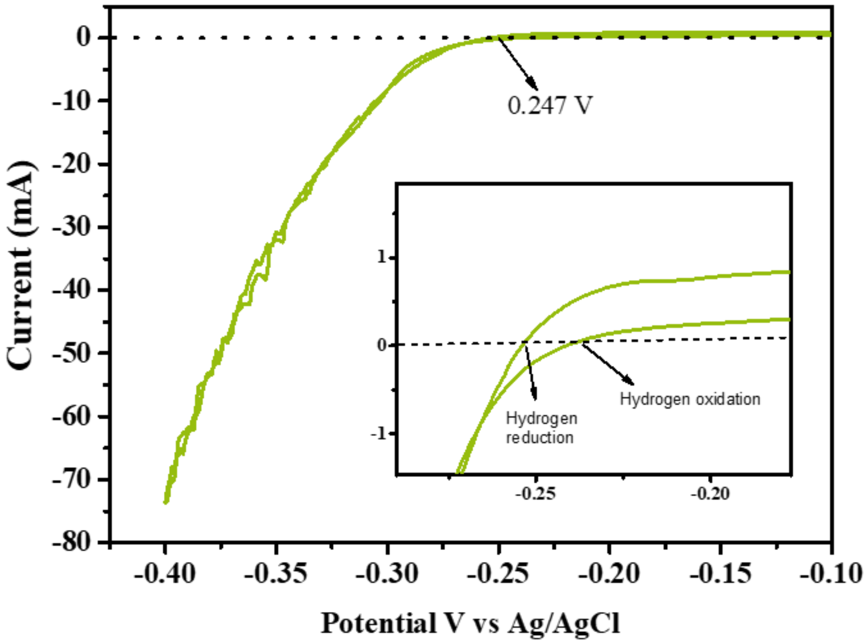

Fig. S9 RHE calibration of Ag/AgCl reference electrode in hydrogen saturated 0.5M H_2SO_4 electrolyte.

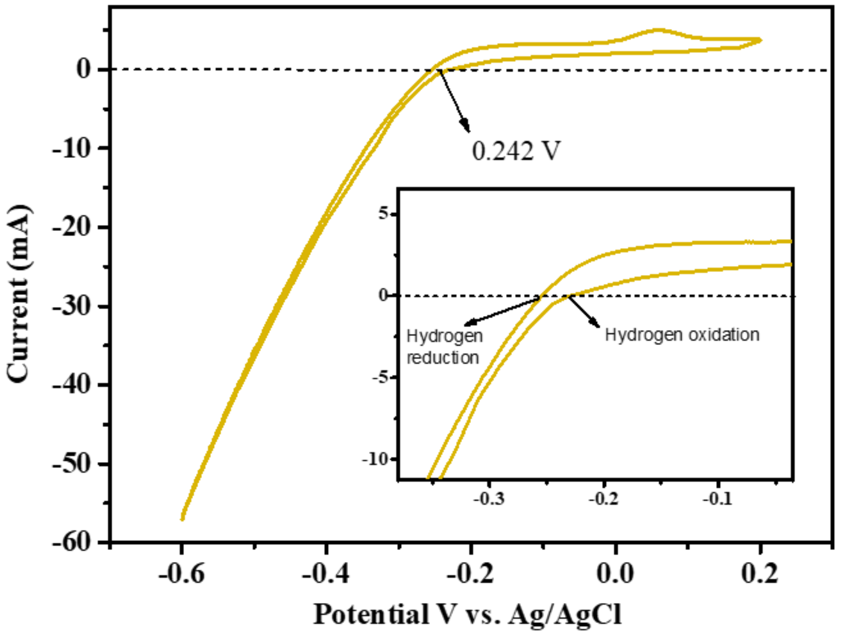

Fig. S10 RHE calibration of reference electrode (Ag/AgCl) in hydrogen saturated 0.5M H_2SO_4 electrolyte used in flow-cell.

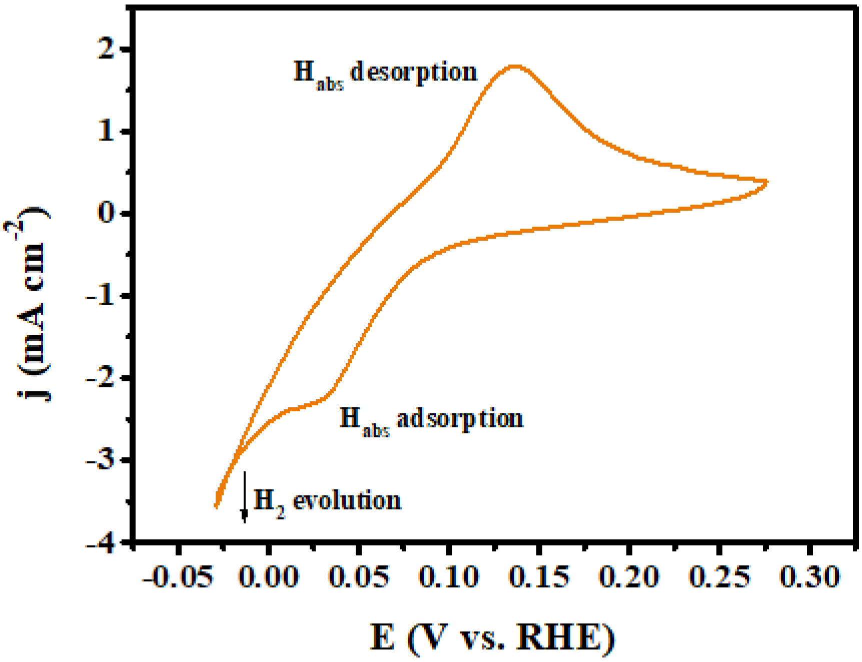

Fig. S11 CV recorded at 5 mVs^{-1} in 0.5 M H_2SO_4.

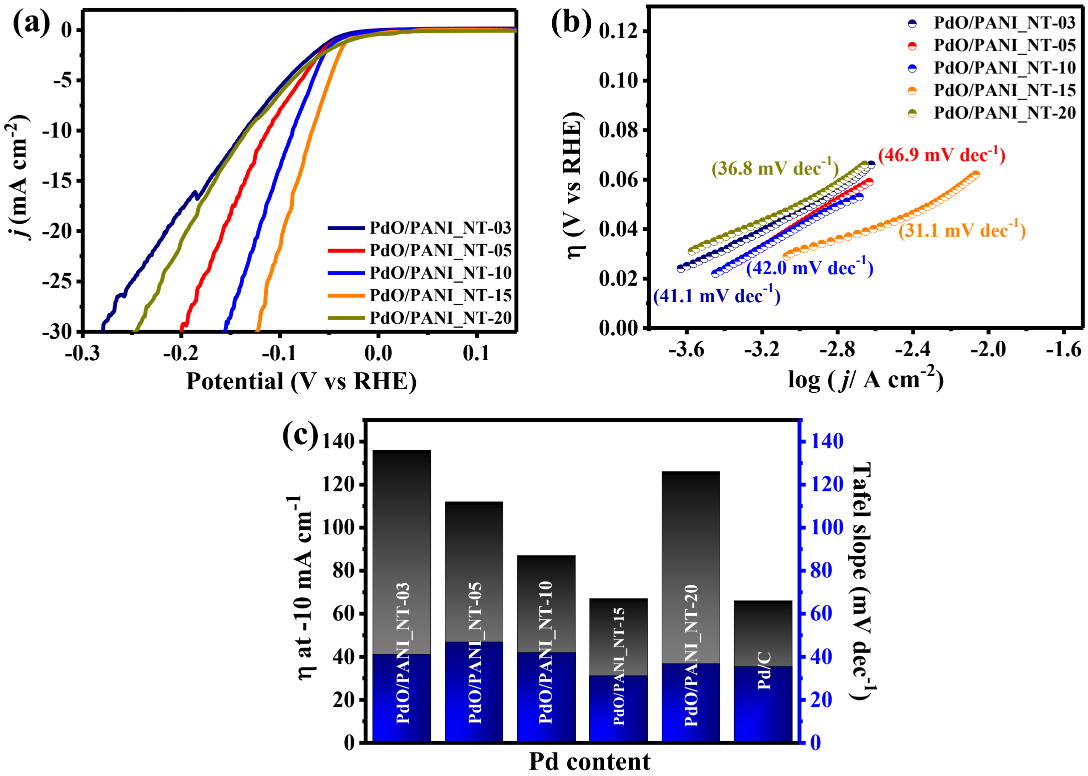

Fig. S12 (a) LSV polarization curves, (b) Tafel slopes of different compositions of PdO/PANI_NT electrocatalysts and (c) comparative bar graph of all series of PdO/PANI_NT samples along with Pd/C.

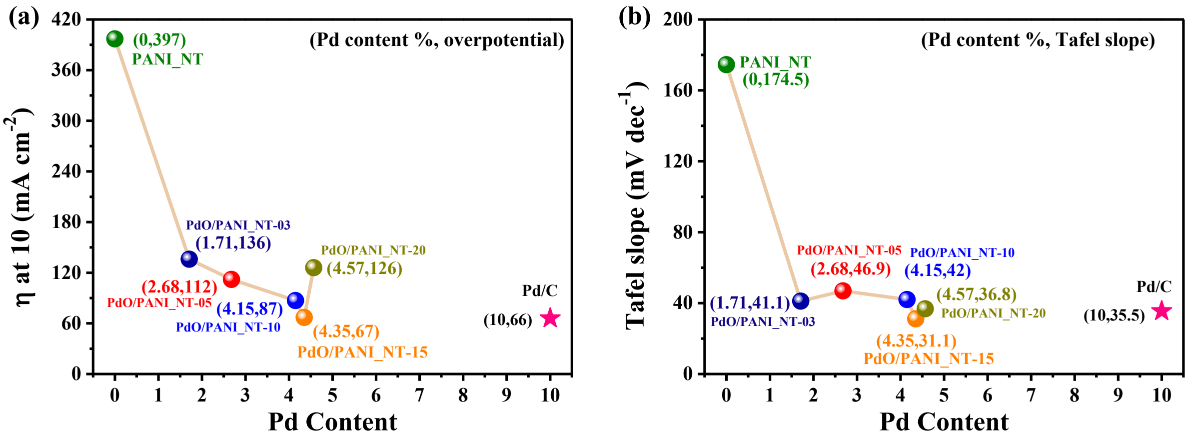

Fig. S13 Comparative graph of (a) overpotential at 10 mA cm^{-2} and (b) Tafel slope with Pd content obtained from ICP-OES of series of prepared catalyst with commercially available Pd/C.

Table S3: Electrochemical performance of different composites of PdO/PANI_NT and Pd/C with Pd-loading % (ICP-OES).

Samples	***Pd loading % (ICP-OES)***	***Tafel slope (mV dec^{-1})***	***Over Potential η_{10} (mV)***
Bare GC electrode	-	192	-
PANI_NT	0	174.5	397
PdO/PANI_NT-03	1.71	41.1	136
PdO/ PANI_NT -05	2.68	46.9	112
PdO/ PANI_NT -10	4.15	42.0	87
PdO/ PANI_NT -15	4.35	31.1	67
PdO/ PANI_NT -20	4.57	36.8	126
Pd/C 10% wt.	10.00 (commercial)	35.5	66

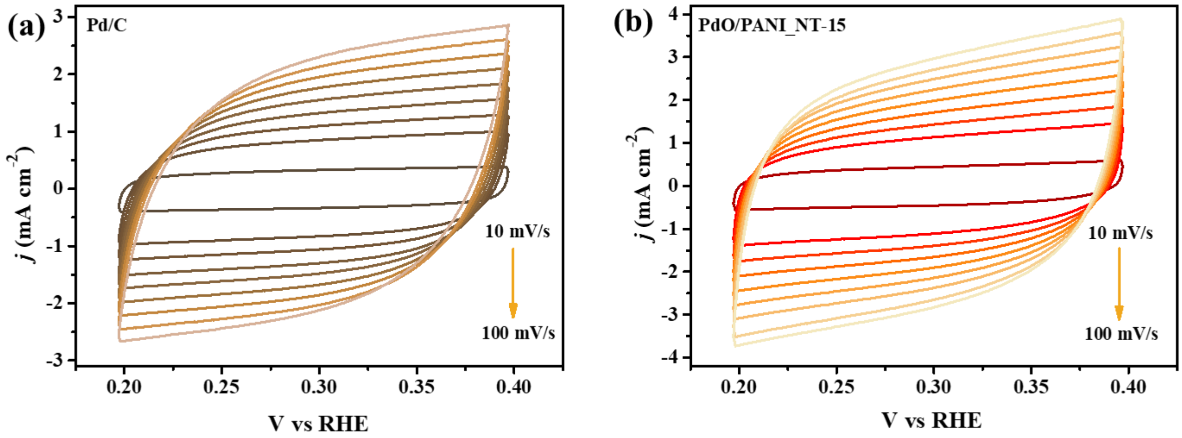

Fig. S14 Cyclic voltammograms (CVs) measured for the (a) Pd/C (b) PdO/PANI_NT-15 at various scan rates with the potential region of non-faradaic current observed in 0.5 M H_2SO_4 electrolyte.

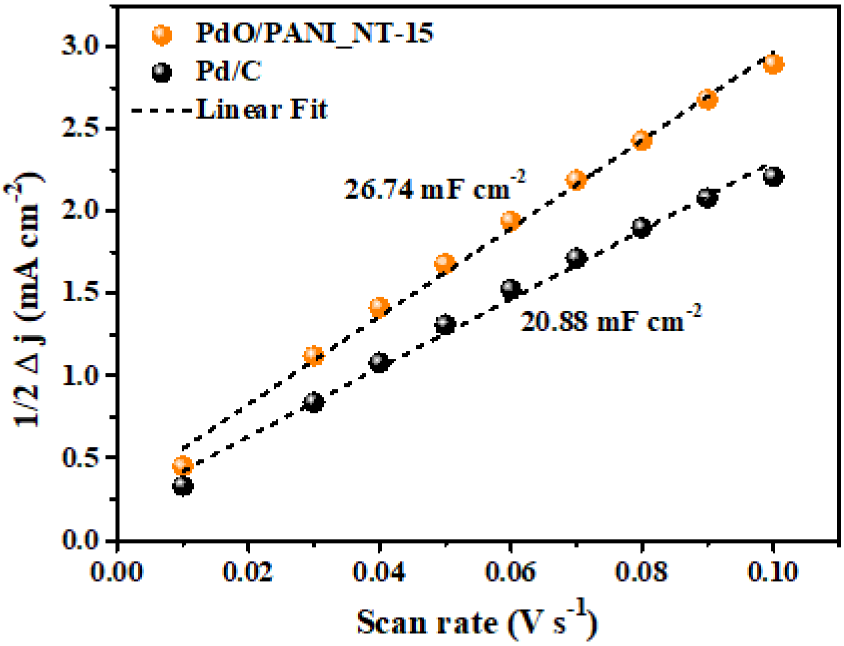

Fig. S15 C_{dl} plots for PdO/PANI_NT-15 and Pd/C.

Table S4: Comparison of HER performance of PdO/PANI_NT-15 and Pd/C.

Catalysts	***Overpotential (mV vs RHE)***		***Tafel (mV dec^{-1})***	***Exchange current density, j_0 (A cm^{-2})***	***C_{dl} (mF cm^{-2})***
	η_{10}	**η_{25}**			
Pd/C	66	113	35.5	2.37×10^{-4}	20.88
PdO/PANI_NT-15 (initial)	67	112	31.1	1.24×10^{-4}	26.74

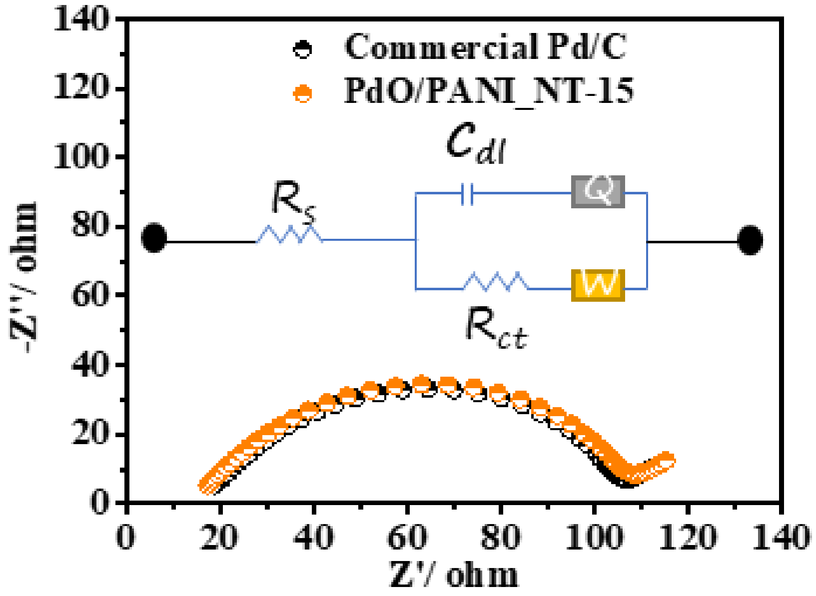

Fig. S16 Nyquist Plots; AC impedance data (at -0.05 V vs RHE with an ac amplitude of 5mV in 0.5 M H_2SO_4 in frequency range of 100 kHz to 10 mHz for PdO/PANI_NT-15, and commercial Pd/C)

Using Electrochemical workstation, the resistance of the catalysts was determined before every experiment by EIS at -0.05 V vs RHE with an ac amplitude of 5mV in 0.5 M H_2SO_4 in frequency range of 100 kHz to 10 mHz for PdO/PANI_NT-15, and commercial Pd/C.

5. ADT and CA tests

The stability of the foremost catalyst, PdO/PANI_NT-15, was studied under dynamic potential scanning (accelerated degradation test, ADT) by continuous run of cyclic voltammetry over the potential range between -0.55 and 0.55 V vs RHE. In comparison to commercial Pd/C, PdO/PANI_NT-15 showed a degradation of only 1.36% from its initial current density, whereas that for Pd/ C was 76.09% after 6000 cycles. (**Fig. 2d and Fig. 2f**)

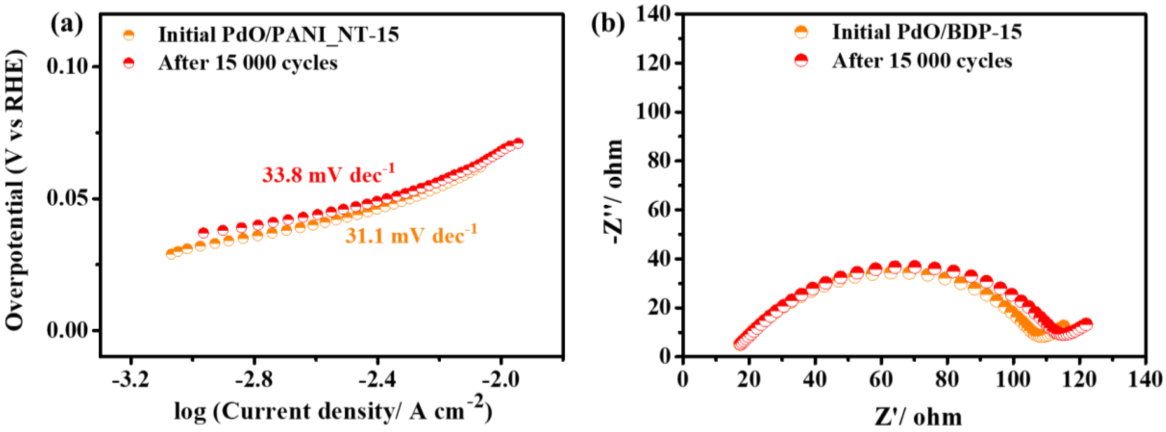

Fig. S17 (a) Tafel slope, and (b) Nyquist plot before and after 15000 CV cycles ADT of PdO/PANI NT-15 composite.

Table S5: Fitting parameters obtained from AC impedance data (fitted with CPE model) for the electrocatalysts in HER

Catalysts	*Solution Resistance R_s (Ω cm^{-2})*	*Charge Transfer Resistance R_{ct} (Ω cm^{-2})*	*Double Layer Capacitance C_{dl} (F cm^{2}) *10^{-6}*	*Warburg Impedance W*	*Constant Phase Element Q*
Pd/C	14.43	88.16	1.248	0.00965	0.0002291
PdO/PANI_NT-15 (initial)	12.90	90.87	1.260	0.00765	0.0002317
PdO/PANI_NT-15 after ADT	13.11	96.73	1.262	0.00720	0.0002276

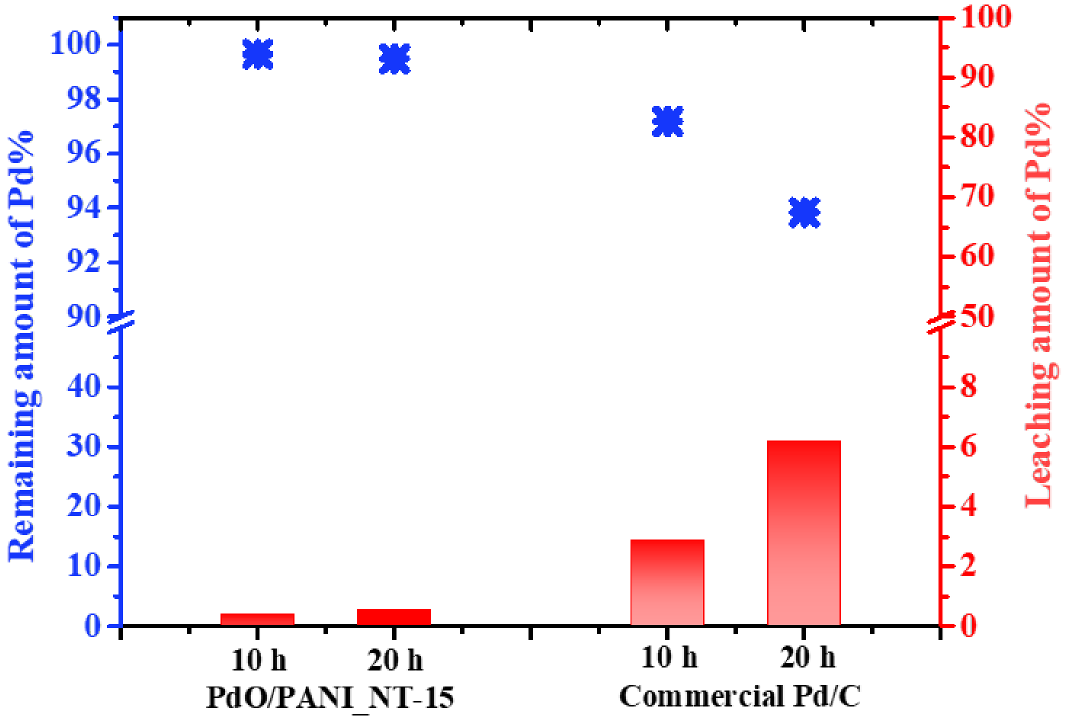

Fig. S18 The leaching of Pd from PdO/PANI_NT-15 and commercial Pd/C as a percentage (right) and remaining amount of Pd (left) during the Chronoamperometry run for different time interval monitored by ICP-OES. (Initial Pd loading were taken as 100 %).

Tabel S6: Leaching amount of Pd into the electrolyte after CA run for different time interval.

Catalysts	***PdO/PANI_NT-15***	***Pd/C***
Pd % (initial)	100 %	100 %
Leaching amount of Pd% (10 h)	0.34 %	2.82 %
Leaching amount of Pd% (20 h)	0.51 %	6.16 %

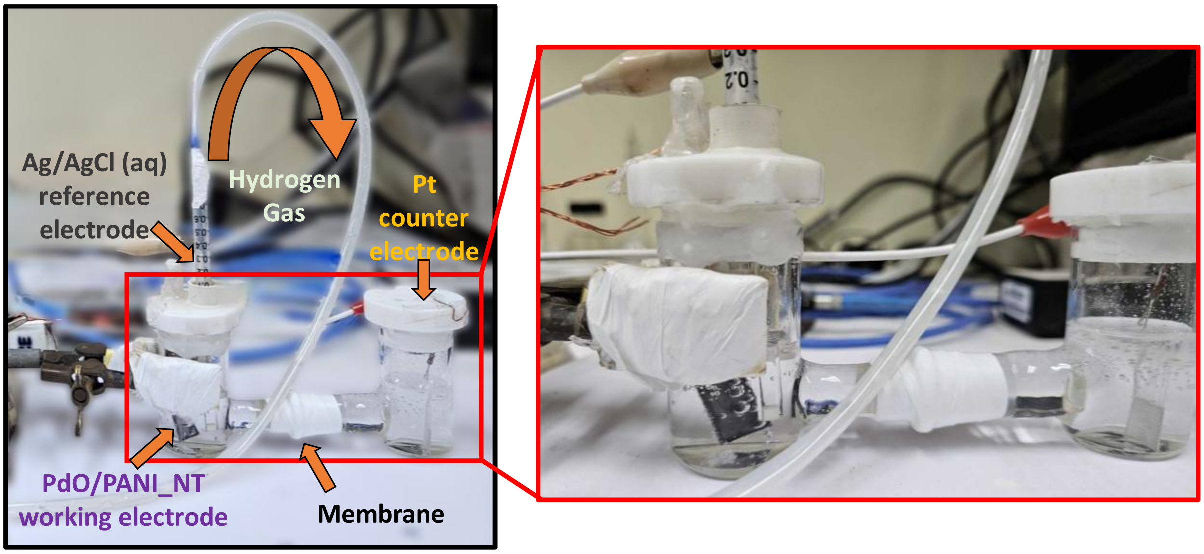

Fig. S19 Schematic representation of custom designed H-cell.

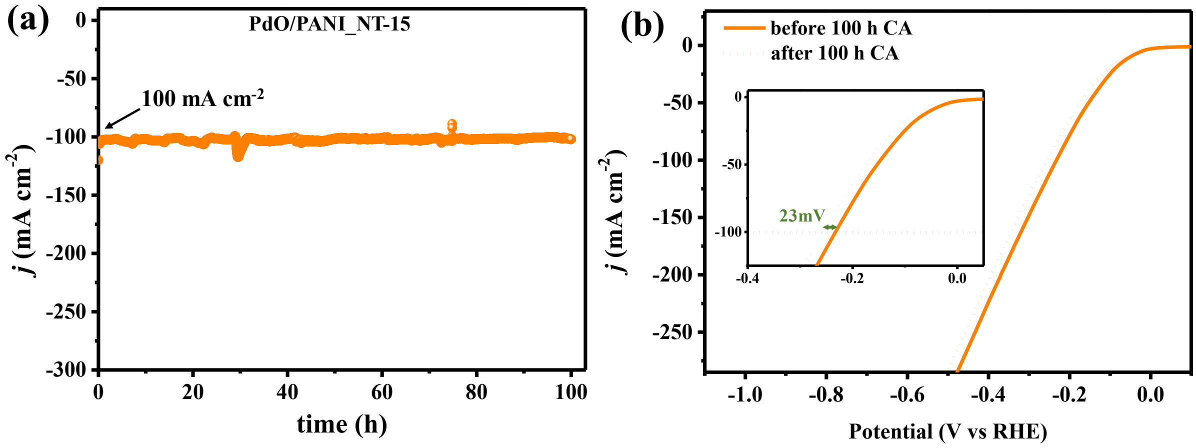

Fig. S20 (a) CA study for PdO/PANI_NT-15 for 100 h at 100mA cm^{-2} current density in 0.5 M H_2SO_4. (b) LSV polarization curve of PdO/PANI_NT-15 before and after CA.

6. Computational Details

Periodic density functional theory (DFT) calculations were performed using the plane-wave technique and as implemented in the Vienna Ab Initio Simulation Package (VASP).[1] The exchange-correlation energy was accounted within the generalized gradient approximation (GGA) method parameterized by the Perdew-Burke-Ernzerhof (PBE) functional.[2] The ion-electron interactions were treated using the projector augmented wave potential (PAW). Grimme's DFT-D2 empirical correction method was employed to describe the van der Waals interactions.[3] All the structures were fully relaxed (both the lattice constant and atomic position). A kinetic energy cut-off was set to be 500 eV, and the convergence threshold was 10^{-4} eV in energy and 0.01 eV/Å in force. The Brillouin zone was sampled with a grid of (1 × 1 × 1) for geometry optimization while a higher Monkhorst–Pack grid of (5 × 5 × 1) was considered for the electronic density of states calculations.

The binding energy (E_b) of PdO and Pd clusters on different surfaces was defined as [4]

$$E_b\ (\text{PdO or Pd}) = E_{(\text{PdO or Pd})/\text{surface}} - E_{\text{surface}} - E_{\text{PdO or Pd}} \tag{S8}$$

The relative free energy of adsorbed atomic hydrogen (H*) was calculated as [4-5]

$$\Delta G_{H*} = \Delta E_{H*} + 0.20 \tag{S9}$$

where H* adsorption energy (ΔE_{H*}) on PdO/PANI_NT and commercial Pd/C composite surfaces were calculated using the following equation:

$$\Delta E_{H*} = E_{H*\text{adsorbed surface}} - E_{\text{surface}} - 1/2E_{H2} \tag{S10}$$

where E_{surface} and $E_{H*\text{adsorbed surface}}$ were total energies of the pristine and H*adsorbed surfaces, respectively and E_{H2} was the energy of gas phase H_2.

Both the doped polyaniline (PANI) and amorphous carbon (a-C) surfaces were modeled based on previous experimental and theoretical studies.[4, 6] A periodic rectangular slabs of cell dimension (19.62 × 11.52 Å^2) with 84 atoms (72 C and 12 N atoms) were considered for polyaniline surface while single-layer amorphous carbon surface was constructed of 120 atoms (96 C and 24 H atoms). Non-planar 3D most stable Pd_8 cluster (as recommended by earlier studies)[7-8] was considered to model Pd/a-C composite mimicking dispersion of Pd nanoparticles on amorphous carbon surface whereas PdO cluster was modelled from the (2 × 2) supercell of bulk PdO considering same number of Pd atoms in the cluster. A vacuum space of 20 Å was used in the direction perpendicular to the surfaces (along Z-direction) to avoid spurious interaction induced by periodic images.

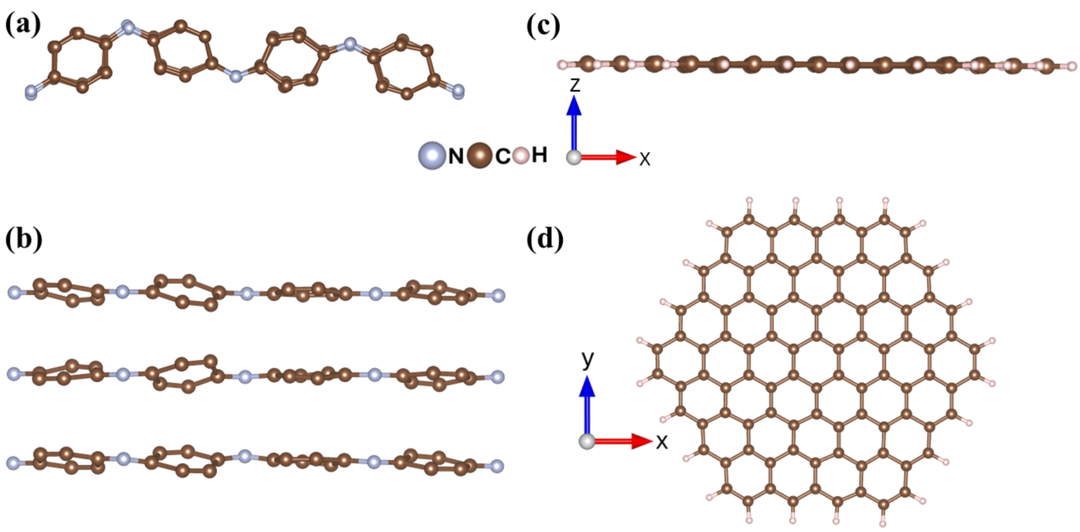

Fig. S21 (a) Optimized structure of (a) side view, (b) top view of PANI_NT surface, (c) side view, (d) top view of amorphous carbon (a-C) surface

Table S7: Formation energy (E_f), hydrogen free energy values ΔG_{H^*} (eV) and d-band centre on different sites of catalyst.

Catalysts	*Formation energy E_f (eV)*	*Adsorption site*	*Free energy ΔG_{H^*} (eV)*	*d-band centre (eV)*
PdO/PANI_NT-15 (initial)	-5.25	Pd (PdO)	0.05	-1.88
		N-site (PANI_NT)	-0.30	
		O-site (PdO)	-0.72	
Pd/C	-0.34	Pd	-0.55	-1.23

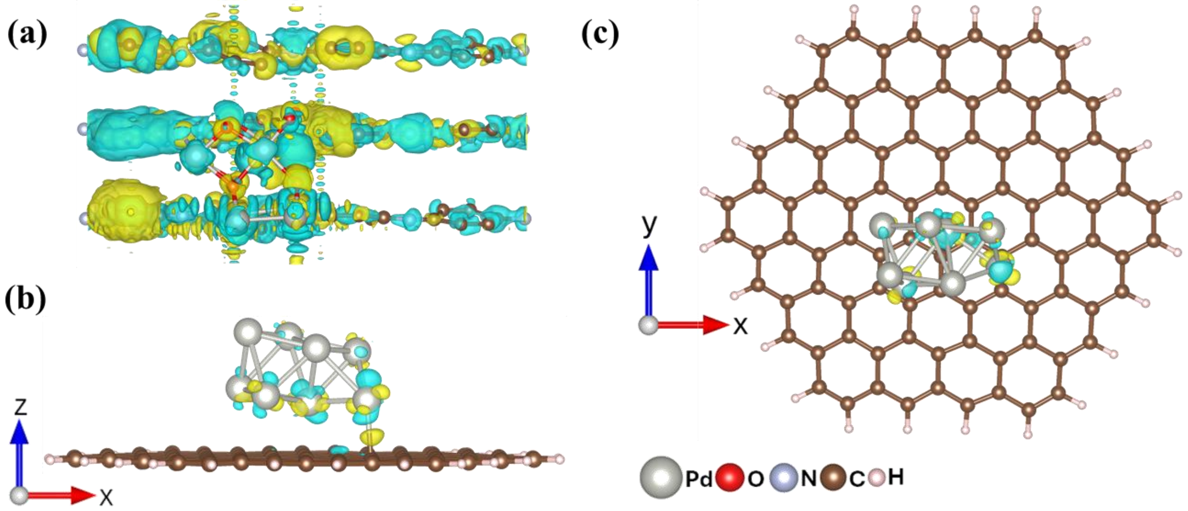

Fig. S22 Charge density difference (CDD) plots (a) top view of PdO/PANI_NT surface, (b) side view, (c) top view of Pd/a-C surface. Isodensity value at surfaces is 0.02 e per a.u.^{3} (positive: olive and negative: cyan) of CDD.

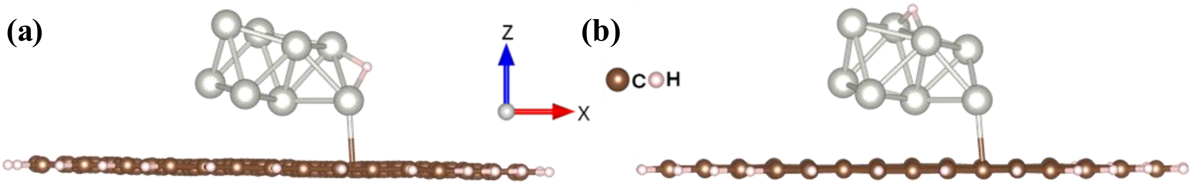

Fig. S23 (a) More stable, (b) less stable H* adsorption Pd-sites on Pd/a-C surface.

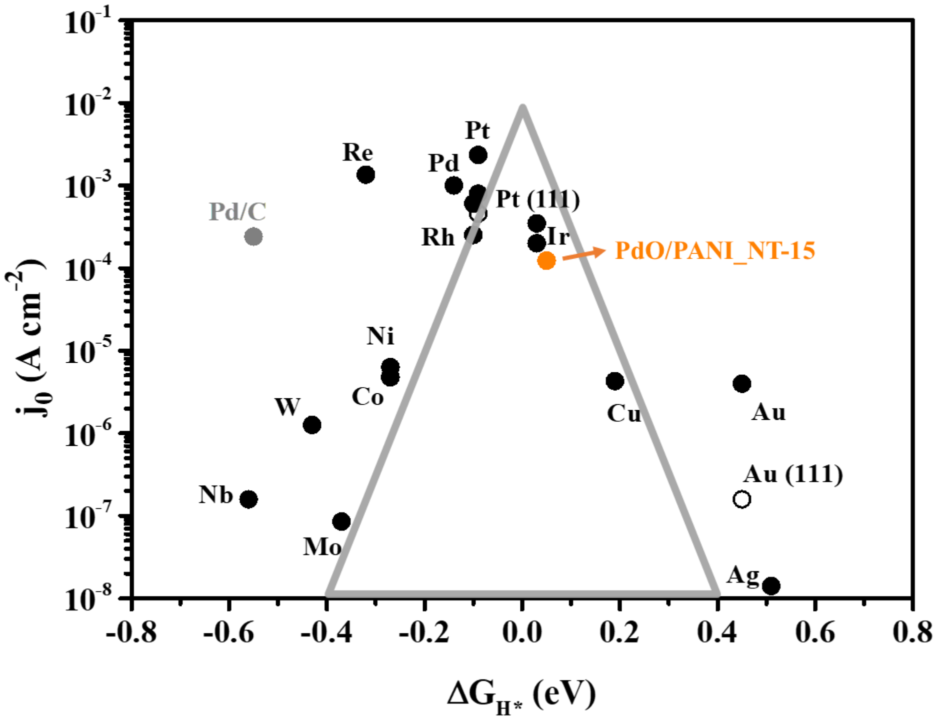

Fig. S24. Volcano plot of HER for PANI_NT-15 and control Pd/C, compared with various pure metals.[9]

7. *In-situ* Electrochemical Fourier Transform-Infrared Spectroscopy (FT-IR)

In-situ electrochemical FT-IR spectroscopy was measured using customed designed cell set up as shown in **Fig. S22** under HER conditions. The measurement was taken 4 cm^{-1} resolution and 100 scans.

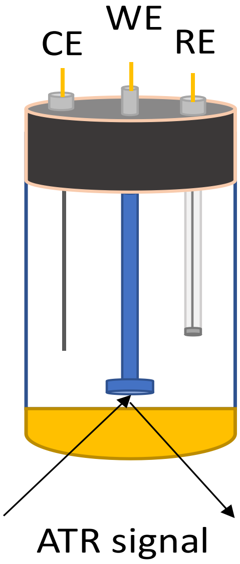

Fig. S25 Schematic illustration of *in-situ* ATR-FTIR configurations.

8. Probing catalyst structure after post-HER and flow-cell H_2 production studies

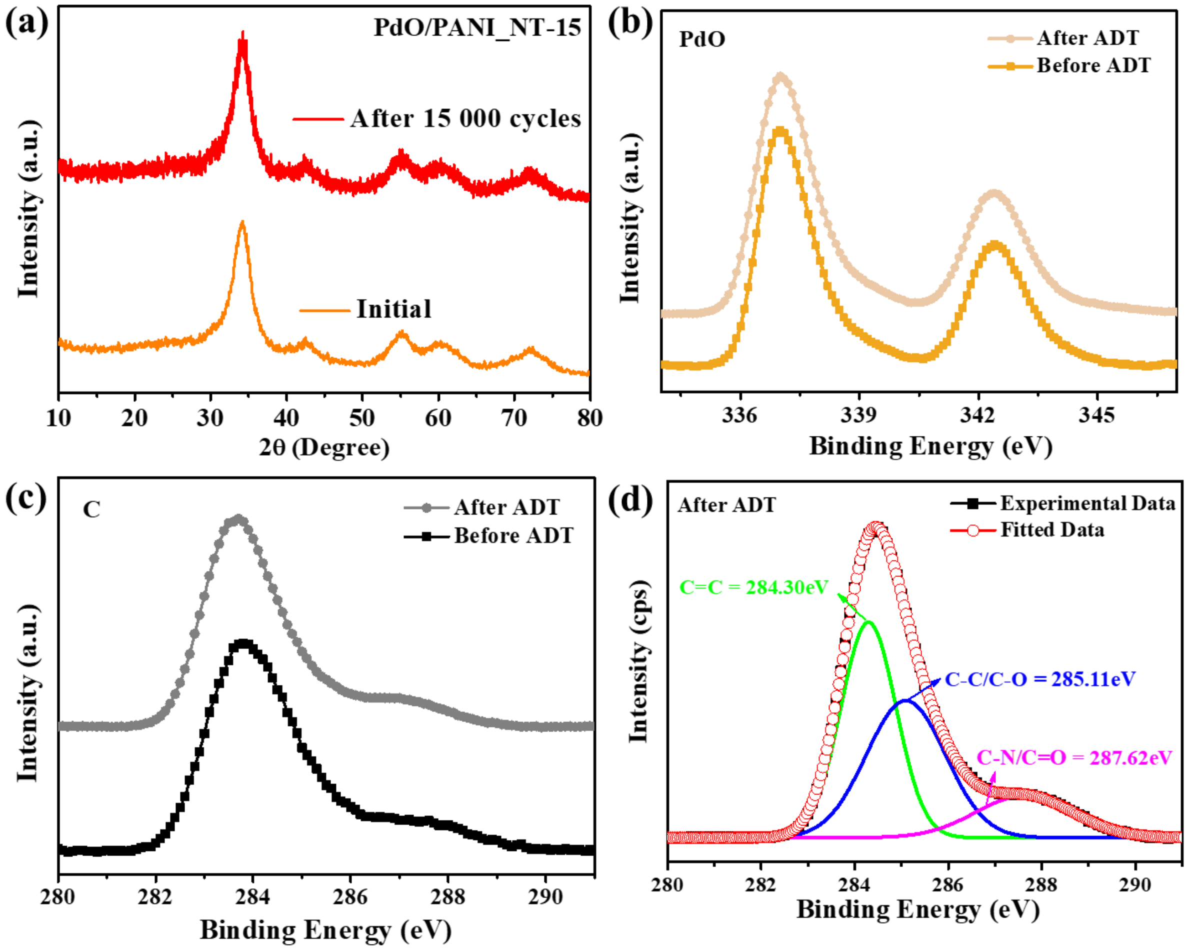

Fig. S26 (a) Comparison of PXRD pattern before and after 15000 CV cycles ADT of PdO/PANI NT-15 composite, (b) Post-HER XPS spectra of Pd 3d (c), C1s and (d) deconvoluted C1s of PdO/PANI_NT-15.

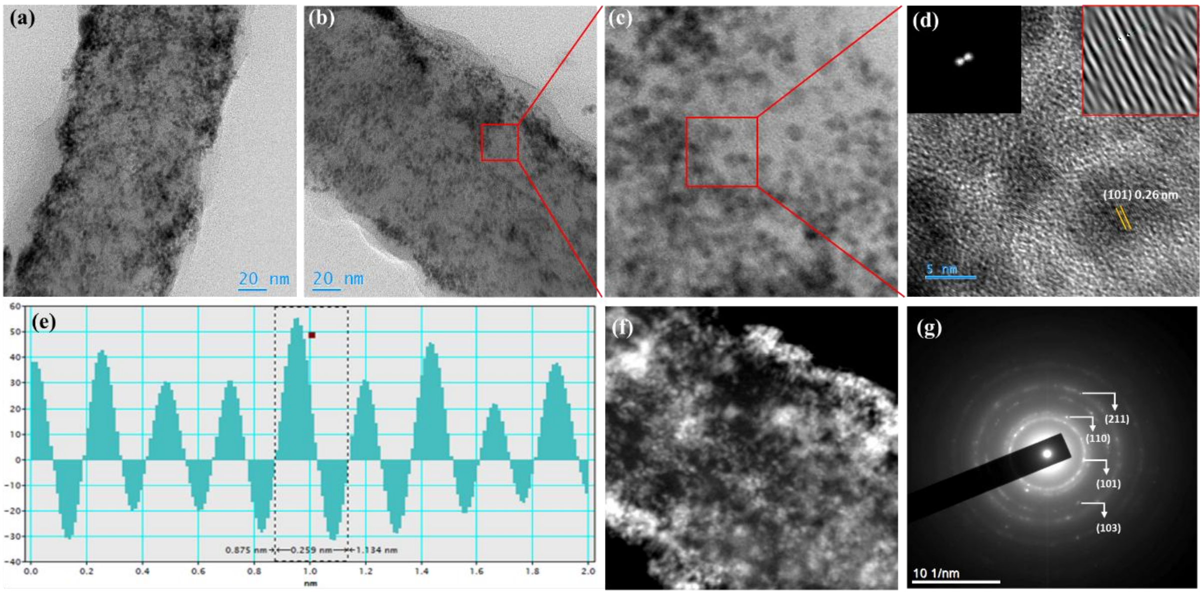

Fig. S27 (a), (b), (c) Post-ADT TEM images of PdO/PANI_NT-15 after 15 000 ADT cycles. (d) HRTEM image (inset: shows the FFT patterns and magnified lattice fringes). (e) the d-spacing of exposed (101) facet of PdO. (f) HAADF-STEM image and (g) SAED pattern for PdO/PANI_NT-15.

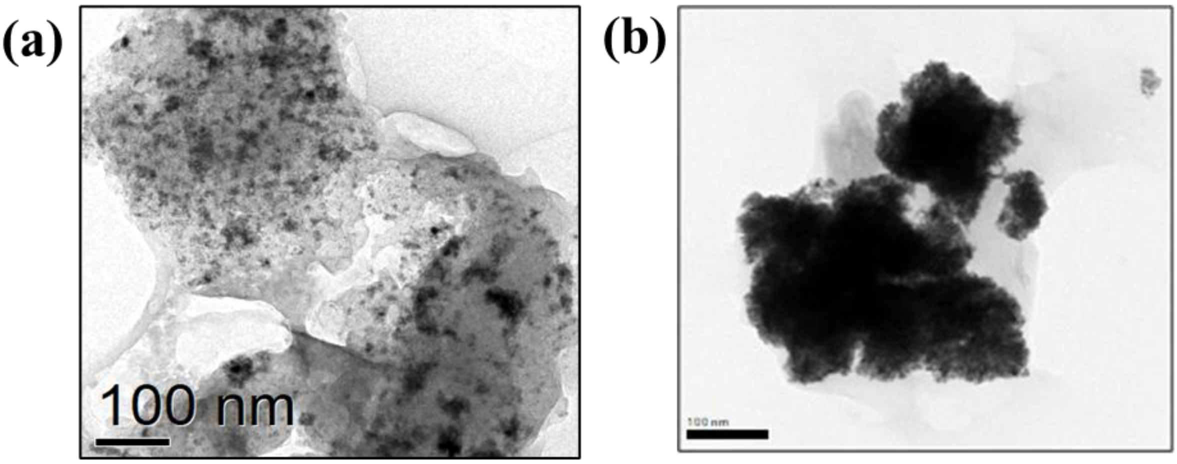

Fig. S28 TEM image of Pd/C (a) before and (b) after 6000 cycles.

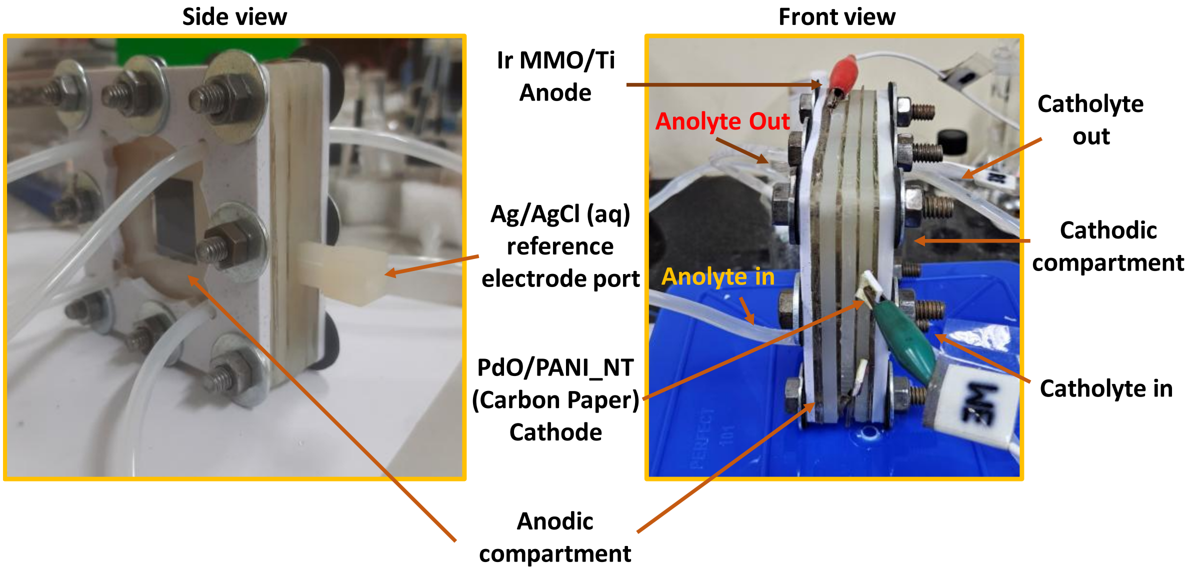

Fig. S29 Schematic representation of custom designed flow-cell setup (dimension of cell: 10×10×3 cm).

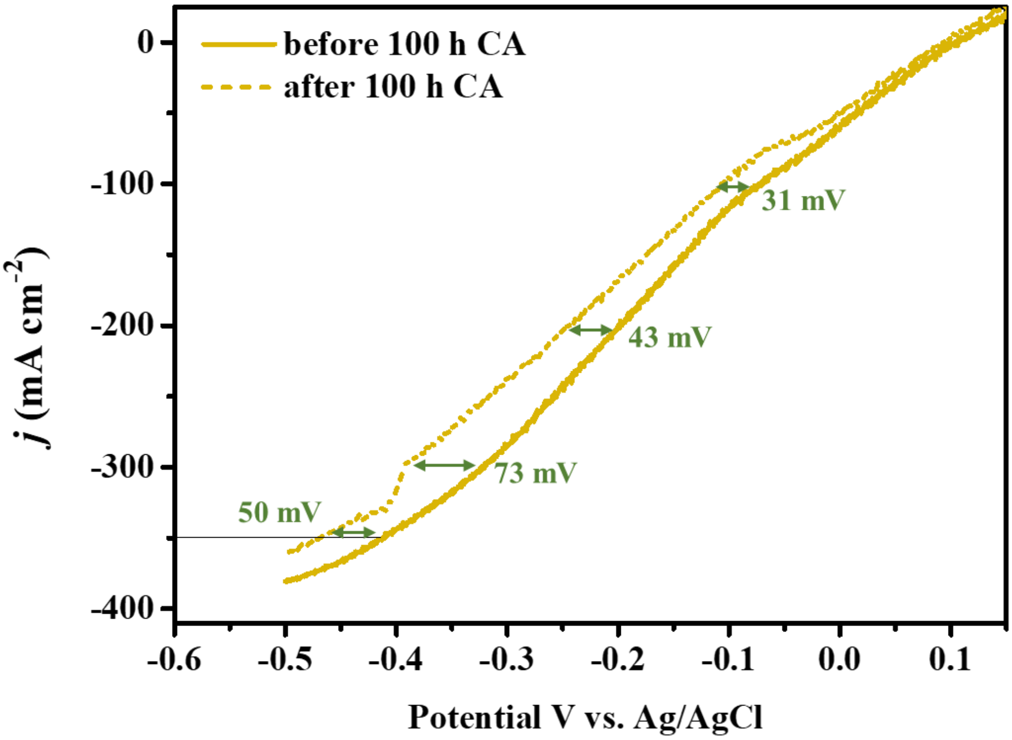

Fig. S30 LSV polarization curve of PdO/PANI_NT-15 before and after CA using flow-cell.

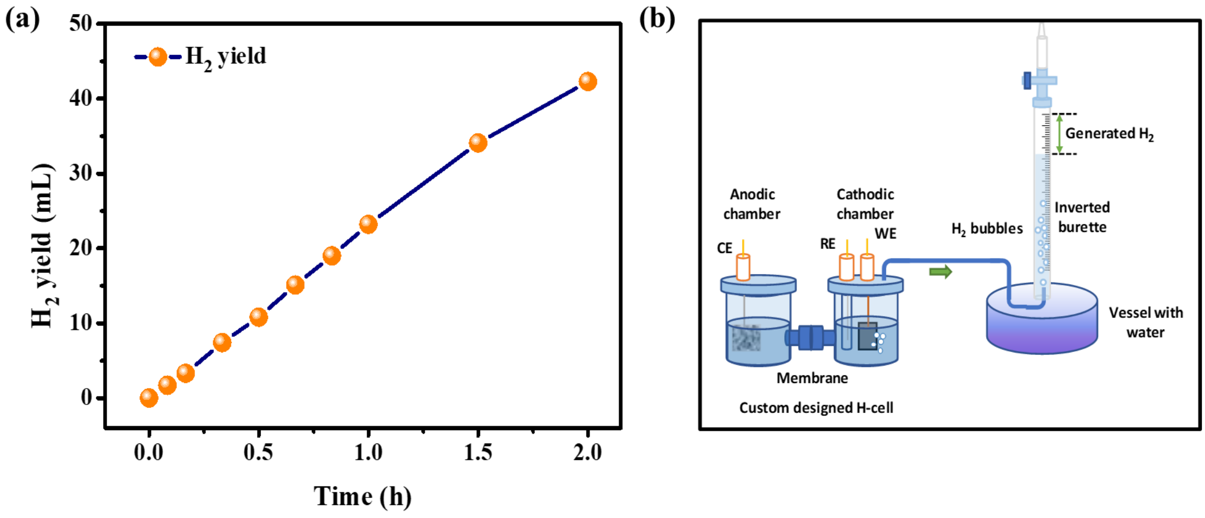

Fig. S31 Hydrogen production quantifies using inverse burette method (a) Hydrogen yield after every instant was quantified during CA run. (b) Schematic of H-cell with H_2 quantification set-up (Please see the media file for more details of H_2 gas evolution).

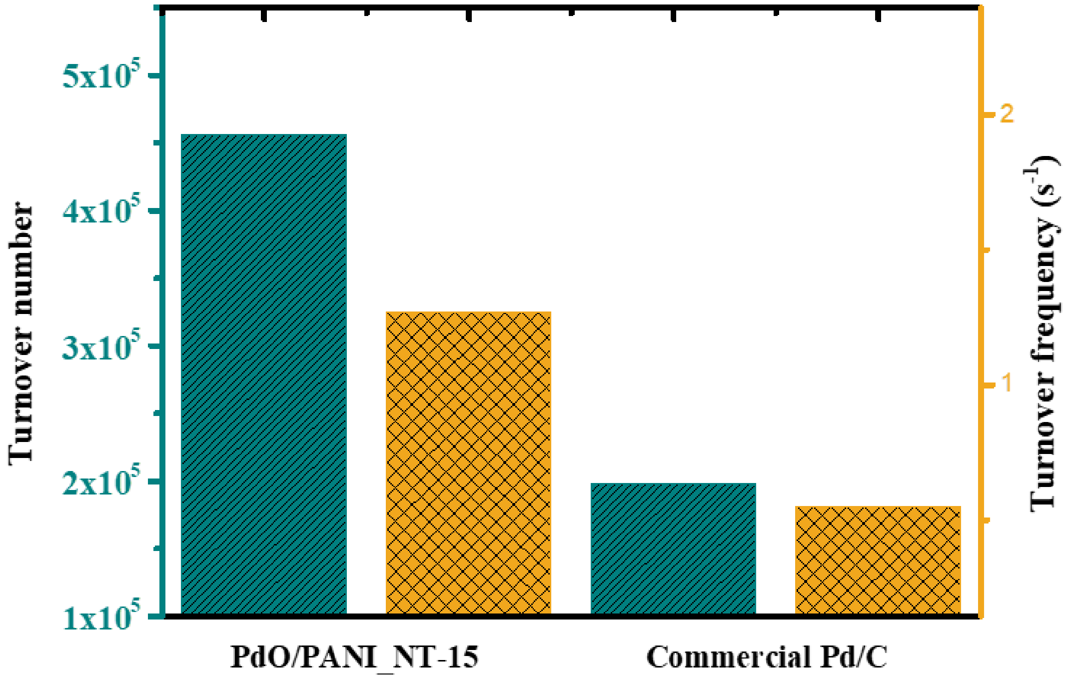

Fig. S32 Turnover number (TON) and turnover frequency (TOF) of PdO/PANI-NT-15 and commercially available Pd/C catalysts.

[The TON and TON of PdO/PANI_NT-15 and control Pd/C catalysts are calculated by the formula of $TON = moles\ of\ evolved\ H_2/(m_{cat.(g)} \times Pd\ wt\%/M_{Pd}(g\ mol^{-1})$ and TOF = TON/t (s), where moles of evolved $H_2 = Q/nF$, m_{cat} is the mass of the catalyst, Pd wt% is taken from ICP-OES, Q is the total charged pass w.r.t time, n is the total electron transfer and F is the faradaic constant.][10-11]

9. Comparative literature surveys

Table S8: The comparison of HER performance of PdO/PANI_NT-15 with Pd and PdO-based materials.

Catalyst	***Tafel slope (mV dec^{-1})***	***Onset overpotential η_{onset} (mV vs. RHE)***	***Overpotential η_{10} (mV vs. RHE)***	***ADT Cycle** (CA time)*	***Reference***
PdO/PANI_NT-15	31.1	22	67	**15000** (>100 h)	**This work**
PdO-400/C	36.4	-	39	-	12
Pd NP CNx	35	12	55	-	13
$Pd_{13}Cu_3S_7$ Nanoplates	49.6	-	64	-	14
Pd/Bi/Cu nano-architectures	61	-	79	-	15
$Pt^{II}{}_2Pd^{II}{}_2Ni^{II}$ complex	-	98	-	-	16
rGO-Pt@Pd	39	39	56	1000	17
rGO-PdPS	46	50	100	1000	18
Pd/MoS_2 nanoflowers	45.2	248	-	1000	19
AgPd alloy decorated MoS_2 Nanosheets	82-109	-	215-229	-	20
PdO–$2Mn_2O_3$	219	-	121		21
ZrO2@PdO NPs	109	-	199 @40 mA cm^{-2}	-	22
PdO/TiO_2	125	-	195	-	23
Pt–PdO–N-doped C	22-36	-	16-29	-	24
PdO-RuO_2/C	34	-	44	-	25
PdNi-S/C nanowires	69.4	-	67	1000	26
Pd@PANI/Au	35	-	60	-	27
AC/PANI-ZnO-NiP	81	-	97	(24 h)	28
NiCu/PANI/NF	41	-	89	(167 h)	29
PANI@Pd/Ni	59	-	111	(10 h)	30
PANI/Ni_2P	52.2	-	137	(350 h)	31
Pd@PANI/Au	35	-	60	(20 h)	32
Pt-NPs supported on N-doped Carbon			50 @ 50 mA cm^{-2}		33
Pt-NPs modified carbon nanofiber	35		47	5000 (12 h)	34

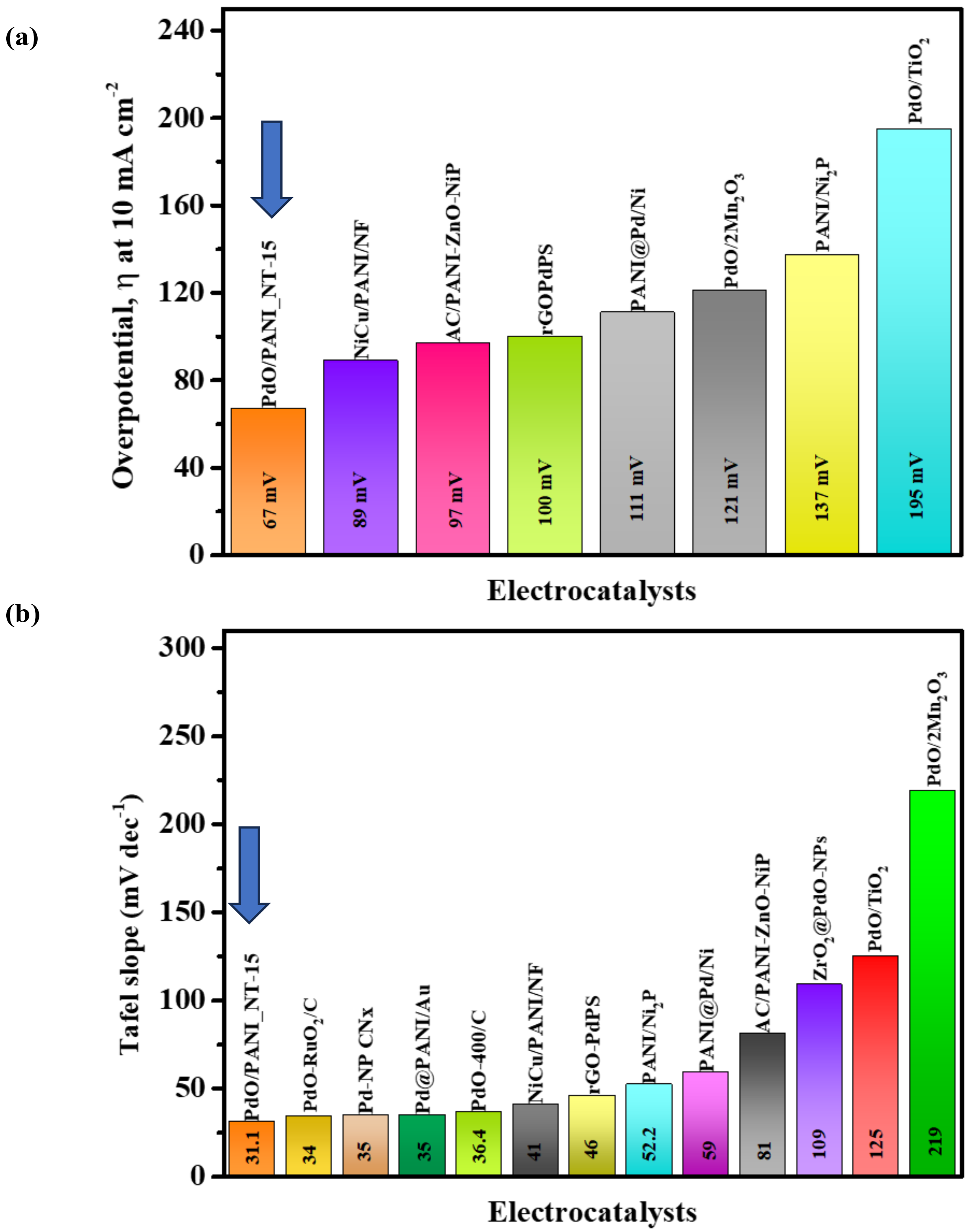

Fig. S33 a) The overpotential and (b)Tafel slope values among PdO/PANI_NT-15 catalyst and other reported HER catalysts. Arrow indicates the obtained value from the current work.

10. References

1. G. Kresse, J. Hafner, *Phys. Rev. B*, 1993, **47**, 558.
2. J. P. Perdew, K. Burke, M. Ernzerhof, *Phys. Rev. Lett.*, 1996, **77**, 3865.
3. S. Grimme, *J. Comp. Chem.*, 2006, **27**, 1787-1799.
4. R. Jana, C. Chowdhury, S. Malik, A. Datta, *ACS Appl. Energy Mater.*, 2019, **2**, 5613-5621.
5. C. Alex, R. Jana, V. Ramakrishnan, M. S. Naduvil Kovilakath, A. Datta, N. S. John, A. Tayal, *ACS Appl. Energy Mater.*, 2023, **6**, 5342-5351.
6. V. Petkov, V. Parvanov, P. Trikalitis, C. Malliakas, T. Vogt, M. G. Kanatzidis, *J. Am. Chem. Soc.*, 2005, **127**, 8805-8812.
7. G. Zanti, D. Peeters, *J. Phys. Chem. A*, 2010, **114**, 10345-10356.
8. Y. Li, C. Liu, Z. Pu, L. Bao, Y. Zhu, J. Ma, *J. Phys. Chem. C*, 2019, **123**, 13739-13747.
9. (C. G. Morales-Guio, L. A. Stern, X. Hu, *Chem. Soc. Rev.*, 2014, **43**, 6555-6569
10. A. Raveendran, M. Chandran, R. Dhanusuraman, *RSC Adv.*, 2023,13, 3843-3876.
11. B. Xiong, L. Chen, J. Shi, *ACS Catal.* 2018, 8, 3688-3707.
12. R. Samanta, R. Mishra, S. Barman, *ACS Sustainable Chem. Eng.*, 2022, **10**, 3704–3715.
13. T. Bhowmik, M. K. Kundu, S. Barman, *ACS Catal.*, 2016, **6**, 1929-1941.
14. J. Park, H. Jin, J. Lee, A. Oh, B. Kim, J. H. Kim, H. Baik, S. H. Joo, K. Lee, *Chem. Mater.*, 2018, **30**, 6884-6892.
15. L. Zheng, S. Zheng, H. Wei, L. Du, Z. Zhu, J. Chen, D. Yang, *ACS Appl. Mater. Interfaces*, 2019, **11**, 6248-6256.
16. A. Döner, F. Tezcan, G. Kardaş, *Int. J. Hydrogen Energy*, 2013, **38**, 3881-3888.
17. X. X. Lin, A. J. Wang, K. M. Fang, J. Yuan, J. J. Feng, *ACS Sustain. Chem. Eng.*, 2017, **5**, 8675-8683.
18. S. Sarkar, S. Sampath, *Chem. Commun.*, 2014, **50**, 7359-7362.
19. B. B. Li, S. Z. Qiao, X. R. Zheng, X. J. Yang, Z. D. Cui, S. L. Zhu, Z.Y. Li, *J. Power Sources*, 2015, **284**, 68-76.
20. M. D. Sharma, C. Mahala, M. Basu, *Chem. Select*, 2019, **4**, 378-386.

21. T. Zahra, K. S. Ahmad, A. G. Thomas, C. Zequine, R. K. Gupta, M. A. Malik, M. Sohail, *RSC Adv.*, 2020, **10**, 29961-29974.
22. T. Zahra, K. S. Ahmad, C. Zequine, R. Gupta, A. Thomas, M. A. Malik, S. Iram, D. Ali, *Int. J. Energy Res.*, 2022, **46**, 8516-8526.
23. M. M. Ibrahim, A. Mezni, M. Alsawat, T. Kumeria, M. R. Das, S. Alzahly, A. Aldalbahi, K. Gornicka, J. Ryl, M. A, Amin, T. Altalhi, *Int. J. Energy Res.*, 2019, **43**, 5367-5383.
24. R. Samanta, R. Mishra, S. Barman, *ACS Sustain. Chem. Eng.*, 2022, **10**, 3704-3715.
25. R. Samanta, R. Mishra, S. Barman, *ChemSusChem*, 2021, **14**, 2112-2125.
26. T. Bhowmik, M. K. Kundu, S. Barman, *ACS Catal.*, 2016, **6**, 1929-1941.
27. J. Bao, W. Liu, Y. Zhou, T. Li, Y. Wang, S. Liang, Y. Xue, C. Guo, Y. Zhang, Y. Hu, *ACS Appl. Mater. Interfaces*, 2019, **12**, 2243-2251.
28. B. K. Urhan, H. Ö. Doğan, T. Ö. Özer, Ü. Demir, *Int. J. Hydrogen Energy*, 2022, **47**, 4631-4640.
29. A. R. Sugandhi, A. Mohammed, S. V. S. Nair, R. Sreenivasan, *New J. Chem.* 2024, **48**, 16278-16288.
30. Q. Liu, C. Shi, Y. Ren, X. Fan, Z. Meng, B. Huang, M. Xu, *Appl. Surf. Sci.*, 2024, **664**, 160266.
31. H. Khoshsang, A. Ghaffarinejad, *Inorg. Chem. Commun.*, 2022, **142**, 109631.
32. H. Shi, J. Qian, X. Hu, *J. Power Sources*, 2024, **596**, 234099.
33. L. Ji, J. Wang, S. Zuo, Z. Chen, *J. Phys. Chem. C*, 2017, **121**, 8923–8930.
34. Y. Zhang, J. Tan, F. Wen, Z. Zhou, M. Zhu, S. Yin, H. Wang, *Int. J. Hydrogen Energy* 2018, **43**, 6167-6176.